Emergent Materials
https://doi.org/10.1007/s42247-025-01243-0

ORIGINAL ARTICLE

Corrosion resistance of a high strength Nickel-free austenitic stainless steel produced by laser powder bed fusion

Sophia Isacco[1] · Sofia Antinozzi[1] · Rahul Kumar Agrawal[1] · Erik T. Furton[2] · Sean P. O'Brien[1] · Alexander T. Helmer[1] · Andrzej Wojcieszynski[3] · Philipp Kluge[4] · Allison M. Beese[2] · Rajeev Kumar Gupta[1]

Received: 23 June 2025 / Accepted: 29 August 2025

Abstract
This study demonstrates the simultaneous achievement of high strength and excellent corrosion resistance in a Ni-free, high N austenitic stainless steel fabricated by laser powder bed fusion (PBF-LB). The formation of a single-phase austenitic structure was confirmed through X-ray diffraction analysis, scanning electron microscopy and energy-dispersive X-ray spectroscopy. Cyclic potentiodynamic polarization tests conducted in 0.6 M NaCl solution at room temperature revealed high breakdown potential (1187 ± 31 mV_{SCE}), indicating excellent corrosion resistance for the additively manufactured Ni-free austenitic stainless steel compared to wrought 316L stainless steel. These findings were further supported by immersion tests in $FeCl_3$ solution. The additively fabricated alloy's yield strength and ultimate tensile strength exceeded 800 MPa and 1 GPa, respectively. The results highlight the potential for developing highly corrosion-resistant, high-strength Ni-free austenitic stainless steel by PBF-LB for possible applications for biomedical implants and structures relating to nuclear energy.

Keywords Additive manufacturing · Ni-free stainless steel · Corrosion · Tensile behavior

1 Introduction

Austenitic stainless steels are among the most commonly used alloys, with applications in diverse fields such as the household, medical, aerospace, marine, power and nuclear industries, due to their attractive combination of mechanical properties and corrosion resistance [1]. One commonly used and researched alloy of this austenitic stainless-steel family is the AISI 316 stainless steel. It Has two major alloying constituents, namely 16.5–18.5 wt% Cr which is responsible for much of the corrosion resistance and ~10 to 13 wt% Ni added as an austenite stabilizer [1]. Replacing Ni with other austenite stabilizers, such as Mn and N, offers several advantages. The primary benefit is cost reduction, as Ni is one of the most expensive alloying elements in stainless steels [2]. Another significant advantage is in biomedical applications, where Ni leaching from implants has been found to be harmful to the host [3–5]. Additionally, Ni containing alloys are more prone to radiation damage in nuclear applications [6–8]. Therefore, replacing Ni with other elements that are more affordable, biocompatible, and less prone to radiation damage is highly desirable.

Attempts have been made to replace Ni with Mn, leading to the development of austenitic steels with high Mn content [9]. However, Mn-rich stainless steels have been reported to show poor corrosion resistance which limits their applicability [10, 11]. N, when present in solid solution, enhances the corrosion resistance of stainless steels by modifying the chemical composition of the passive film and improving repassivation in case of passive film breakdown [10, 12–15]. Additionally, N is a potent austenite stabilizer and solid solution strengthener [1], and its solubility increases with increasing Mn content [4, 16]. Further, the corrosion resistance of Ni- free, Mn-containing austenitic stainless

✉ Rahul Kumar Agrawal
rkagrawa@ncsu.edu

✉ Rajeev Kumar Gupta
rkgupta2@ncsu.edu

[1] Department of Materials Science and Engineering, North Carolina State University, Raleigh, NC, USA

[2] Department of Materials Science and Engineering, Pennsylvania State University, University Park, PA, USA

[3] Wingens Consultants, LLC, Pittsburgh, PA, USA

[4] Swiss Steel Group, Carol Stream, USA

Published online: 18 September 2025

steels has been reported to increase by alloying with N [17]. Ni-free, Mn-containing austenitic stainless steels with less than 0.2 wt% N exhibits poor corrosion resistance, while those with higher N content (typically > 0.2 wt%) are known to show enhanced corrosion resistance, often surpassing that of 316L austenitic stainless steel [18–20].

Despite its beneficial effect, the solid solubility of N in stainless steel is Limited, making production of such steels using conventional ingot metallurgy or powder metallurgy processes challenging. At room temperature the maximum achievable solid solubility of N in austenite is reported to be approximately 0.4 wt% [16]. Theoretically, high N partial pressure during melting along with alloying additions of Mn and Mo can result in increase of N solubility up to ~3 wt% in molten iron, at or above 1600°C [16]. Thus, achieving high N content requires melting of steels under high N pressure, followed by fast cooling to retain dissolved N in solid state. Additive manufacturing techniques offer a potential solution in achieving both the above conditions. While manufacturing ferrous materials by powder bed fusion with a laser beam (PBF-LB), the melt pool experiences extremely high temperatures (in the range of 2000–3000 °C) and very fast cooling rates (10^6 K/s) [21, 22]. At such high temperatures, the melt pool can dissolve large amounts of N, which can be subsequently retained upon rapid cooling. Therefore, PBF-LB could be a method to produce ferrous materials with high amounts of N.

Recently, Vukkum et al. [23, 24] have shown that the PBF-LB method using nitrides as additives can produce high-N steels. Similarly, Cheng et al. [25], fabricated high N stainless steels using metal nitride powders followed by PBF-LB. Interestingly, while Vukkum et al. [23] reported a significant improvement in corrosion resistance (breakdown potential of ~1 V_{SCE} in 3.5 wt% NaCl), Cheng et al. [25] did not observe any improvement in passivation. Tochiro et al. [26] successfully optimized the PBF-LB parameters and fabricated high Mn and high N, Ni-free austenitic stainless steels with a tensile strength of ~1.2 GPa. However, the corrosion behavior of these steels remains relatively unexplored.

Given the importance of achieving both high strength and excellent corrosion resistance in structural alloys, we report herein the corrosion and mechanical properties of Ni-free, high N austenitic stainless steel manufactured using gas-atomized powders (commercially available as Printdur® HSA) and PBF-LB. In the present work, Mn and N serve as austenite stabilizers. A comprehensive analysis of the corrosion performance and tensile behavior of Ni-free, additively manufactured austenitic stainless steel is presented and compared with that of 316L wrought stainless steel.

2 Materials and methods

2.1 Sample preparation

Samples of additively manufactured high N, Ni-free stainless steels (hereafter referred to as "AM Ni-free") were received in the as-printed condition from Swiss Steel Group. The powders (commercially available as Printdur®) used for additive manufacturing were gas-atomized in N_2. The AM Ni-free samples were subsequently fabricated using these powders on an EOS M290 3D printer using a 240 W laser power at a scan speed of 930 mm·s^{-1} and with a Hatch distance of 0.1 mm (energy density ~ 80 J·cm^{-3}). Details about the optimized parameters are given in [26]. Wrought 316L stainless steels ("W-316L") was also used for comparison. The chemical composition (in wt%) of a typical 316L stainless steel and AM Ni-free stainless steel used in this study are presented below in Table 1.

2.2 Characterization

All samples were ground to 1200 grit surface finish with SiC abrasive paper and rinsed with ethanol prior to any characterization. X-ray diffraction (XRD) was conducted using a Rigaku SmartLab X-Ray Diffractometer with Cu-Kα radiation (λ = 1.541862 nm), covering a 2θ range of 25° to 120°, with a step size of 0.02°. Bragg-Brentano geometry focusing was used.

Scanning electron microscope (SEM) imaging was performed using a Hitachi Ultrahigh-Resolution Schottky Scanning Electron Microscope SU8700. SEM imaging was conducted prior to electrochemical testing. For this, samples were ground and polished to a fine finish of 0.05 µm using a diamond suspension and an alumina polishing solution. After polishing, the AM Ni-free sample was electro-etched with 10% oxalic acid at 15 V for 60 s, according to the ASTM A262 Practice-A. SEM was conducted on both the unetched and etched AM Ni-free sample to observe the presence of melt pools, grain boundaries, and cell boundaries.

For examination of finer microstructural details, electron transparent lamellae were analyzed using a transmission electron microscope (TEM) (Talos F200X fitted with Super-X

Table 1 Chemical composition of specimens in wt.%

	Cr	Mn	Si	Mo	C	*N*	Ni	Fe
W-316L	16.5	1.2	0.27	2.0	< 0.02	< 0.1	10.0	bal.
AM Ni-free	18.0	21.0	0.2	3.0	0.4	0.6	–	bal.

EDS detector). The electron transparent lamellae were prepared using focused ion-beam (FIB) lift out technique in a dual beam scanning electron microscope (Scios 2).

2.3 Electrochemical testing

All electrochemical tests were conducted on ground samples in a 0.6 M NaCl solution at room temperature using an electrochemical workstation (Biologic VMP300). A three-electrode cell with a saturated calomel reference (SCE) and platinum mesh counter electrode (CE) were used. The open circuit potential (OCP) was recorded for an hour before polarization tests. Cyclic potentiodynamic polarization (CPP) tests were conducted from 0.200 V below OCP with a step size of 1 mV/s. The potential was reversed when either potential reached 1500 mV_{SCE} or current density reached 250 $\mu A/cm^2$. $FeCl_3$ droplet testing was conducted at room temperature as per the ASTM G48-11 Practice-A, using a 6 wt% $FeCl_3$ solution. The test was conducted for two hours, on an AM Ni-free sample and W-316L sample for comparison. The exposed sample area was 0.079 cm^2 and all the electrochemical tests were repeated thrice.

2.4 Mechanical testing

Net-shaped uniaxial tension samples were designed with the geometry shown in Fig. 1, with the build direction parallel to the loading direction. Mechanical tests were conducted on six samples with a universal testing machine (Criterion Model 45, MTS, Eden Prarie, MN) under a quasi-static loading rate of 10^{-3} s^{-1}. Displacement was measured with noncontact stereographic digital image correlation (VIC 3D, Correlated Solutions, Irmo SC), using a virtual extensometer with an initial length of 24 mm.

3 Results

3.1 Microstructural characterization

The X-ray diffraction profile of the AM Ni-free stainless steels is presented in Fig. 2. The XRD results primarily indicate an austenite phase. Additionally, smaller peaks appear at lower Bragg angles of the (111) and (200) austenite reflections. According to the ICSD database these peaks correspond to a type of Mn-Si-O phase, either in cubic ($Mn_5Si_3O_{12}$, ICSD 00-037-0221) or orthorhombic (Mn_2O_4Si, ICSD 00-035-0748) crystal structures. The formation of such Mn-Si-O rich inclusions has been identified in the electron micrographs of other additively manufactured stainless steels [23, 27]. No peaks indicating the presence of δ-ferrite or α-martensite are observed.

The electron micrographs of stainless steel under investigation, in both etched and un-etched conditions, are presented in Fig. 3. As seen in Fig. 3(a) complete fusion between successive passes and a dense microstructure are evident. The secondary electron micrographs (Fig. 3 (b to d)) show the typical microstructure of an additively manufactured stainless steel. Melt pools, equiaxed and columnar cells, and cellular sub-structures are visible. The melt pools vary in size, with more variability in width than in depth. The dimensions of the melt pool are known to be a function of the additive manufacturing technique and processing parameters used [23, 28, 29]. Cells containing equiaxed and columnar sub-cells were observed within the melt pools. The cell boundaries are regions of high dislocation density and/or elemental segregation, separating nearby regions with low dislocation densities [23, 29]. The shapes of cells in the micrographs depend on the relationship between the thermal gradient of the solidification front and the plane in which the micrograph was taken. When the thermal gradient is normal to the plane of micrograph, the sub-cells appear 'equiaxed.' In contrast, when the thermal gradient is in the plane of micrograph, the cells appear 'columnar.'.

Interestingly, Mn-Si-O phase identified by the XRD was not detected through SEM/EDS analysis (Fig. 3 and Supplementary Figure S1, refer to electronic supplementary material). Therefore, S/TEM EDS mapping was performed (Fig. 4). Fine Mn-Si-O rich particles were observed under S/TEM (Fig. 4 and Supplementary Figure S2, refer to electronic supplementary material), which confirmed XRD results. As shown in the S/TEM micrograph (Fig. 4 and Supplementary Figure S2), the size of such Mn-Si-O particles Had diameters on the order of 50 nm, which explains their non-detection in SEM EDS, although a detailed quantitative analysis for the Mn-Si-O particle size distribution has not been conducted.

3.2 Corrosion behavior

The cyclic potentiodynamic curves (CPP) of AM Ni-free and W-316L stainless steels are presented in Fig. 5. Both alloys exhibit spontaneous passivity and the current density in the passive region is similar for the two alloys. Current transients (indicative of metastable pitting) were observed in W-316L, whereas AM Ni-free stainless steel did not show any current transients in the passive region. The corrosion potentials of the two alloys were similar. The breakdown potential (E_b) for the AM Ni-free stainless steel was 1187 ± 31 mV_{SCE}, which is significantly higher than that for the W-316L (546 ± 20 mV_{SCE}). Further, the repassivation potential (E_{rep}) for the AM Ni-free stainless steel (1015 ± 39 mV) was also higher compared to W-316L (129 ± 17 mV).

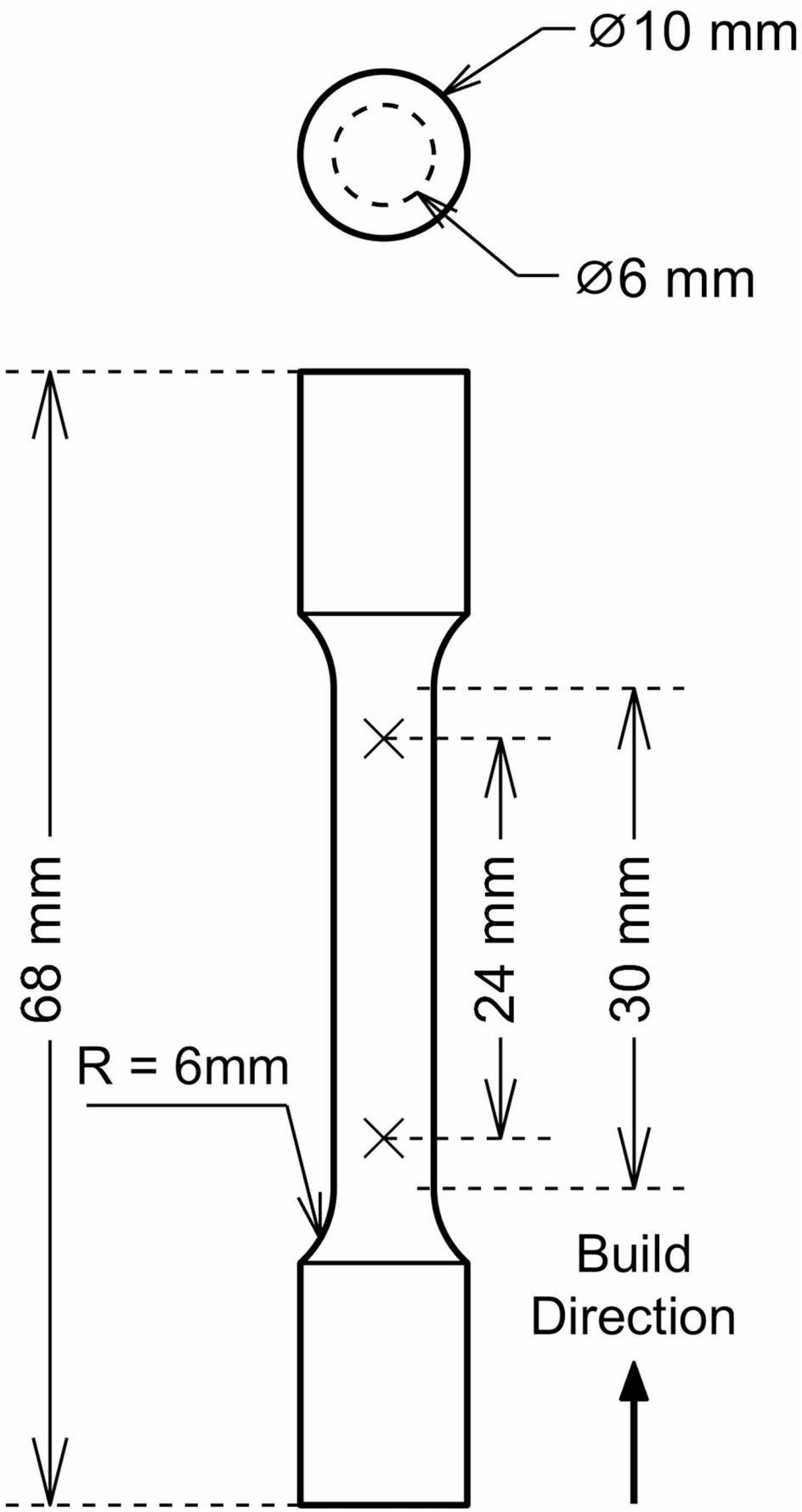

Fig. 1 Geometry of uniaxial tension sample. The displacement was measured with a virtual extensometer, with endpoints marked with 'x' labels

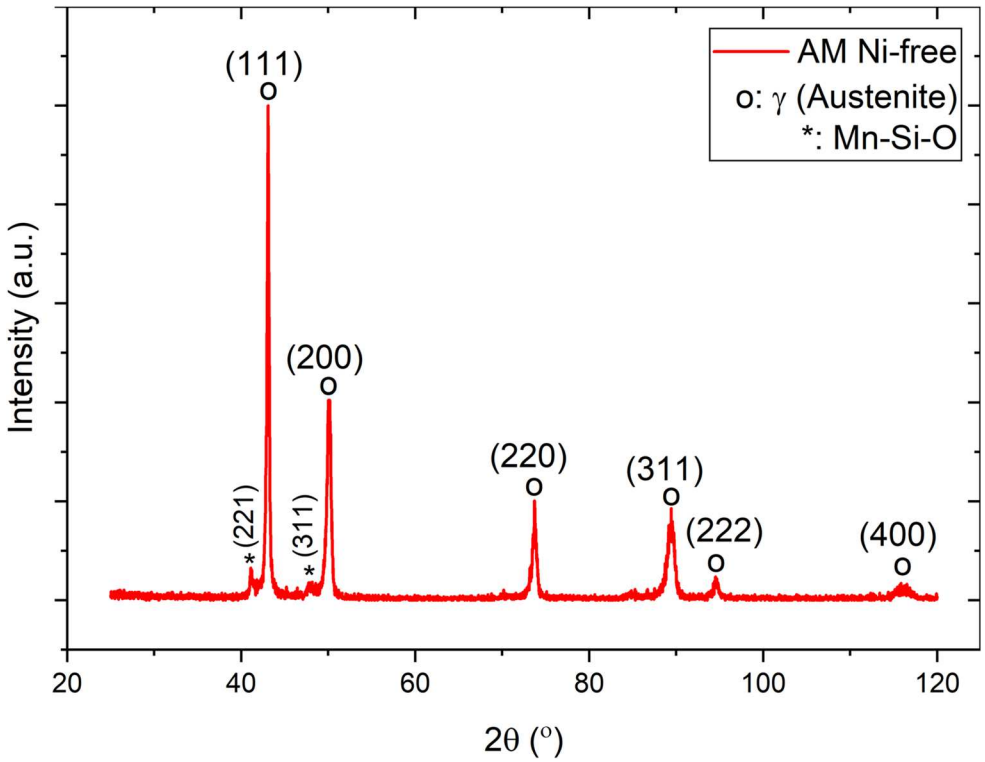

Fig. 2 X-ray diffractogram of the as-printed AM Ni-free stainless steel indicating predominantly an austenitic phase with secondary Mn-Si-O peaks

For materials prone to pitting corrosion, the breakdown potential (E_b) is observed to be more noble than the repassivation potential (E_{rep}). Also, the difference between E_b and E_{rep} follows an inverse relationship with the material's susceptibility to pitting corrosion, i.e. a more resistant material shows smaller value for E_b-E_{rep} [30]. Notably, the E_b-E_{rep} for AM Ni-free (172 mV) is much smaller when compared to W-316L (417 mV). The area between the forward scan and the reverse scan in the CPP plots is termed the hysteresis loop and is used as a measure of pitting corrosion resistance [30–32]. A larger hysteresis loop indicates a higher propensity for pitting corrosion. The hysteresis loop for AM Ni-free stainless steel is significantly smaller than that in W-316L, indicating a higher resistance to pitting corrosion.

The AM Ni-free stainless steel exhibited higher breakdown and repassivation potentials, a larger passive width (the difference between breakdown and corrosion potentials), absence of current transients in the passive region, and a lower hysteresis loop, indicating significantly higher corrosion resistance compared to W-316L [30–32]. $FeCl_3$ testing was further conducted, which corroborated the conclusions from the CPP. Stereoscope images of AM Ni-free stainless steel and W-316L after $FeCl_3$ testing are presented in Fig. 6. The W-316L sample appears to exhibit greater deterioration than the AM Ni-free stainless-steel sample, again indicating that the AM Ni-free stainless steel is more resistant to corrosion.

3.3 Tensile behavior

The engineering stress-strain behavior of the AM Ni-free alloy is shown in Fig. 7a, and the mechanical properties are reported in Table 2. The mechanical behavior is compared to a wrought nickel-free alloy [33], and to both PBF-LB and wrought SS316L [34, 35]. Compared to wrought Ni-free austenitic stainless steel, the AM Ni-free stainless steel had greater strength and reduced ductility. In addition to the supersaturation of N in the FCC matrix, micro segregation cells impede dislocation motion and contribute to strengthening. Due to the increased interstitial content, the strength of Ni-free alloy was greater than that of SS316L.

Hsiao and Dullis [36] showed that for Cr-Mn-C-N steels, the effect of interstitial C and N on the yield strength could be approximated as:

$$YS\ (MPa) = YS_0\,(MPa) + 338\,(C\ wt.\,\%) + 405(N\ wt.\,\%) \quad (1)$$

where YS_0 is the yield strength in the absence of these alloying interstitials. YS_0 and the strengthening due to interstitials are compared in Table 2. Both AM Ni-free and SS316L have approximately the same value of YS_0, while the Ni-free alloy's contribution from interstitials was greater than SS316L's by over 300 MPa. This indicates that the strengthening due to grain and cell boundaries is comparable, but the additional C and N in the Ni-free alloy provides nearly all the additional strength compared to additively

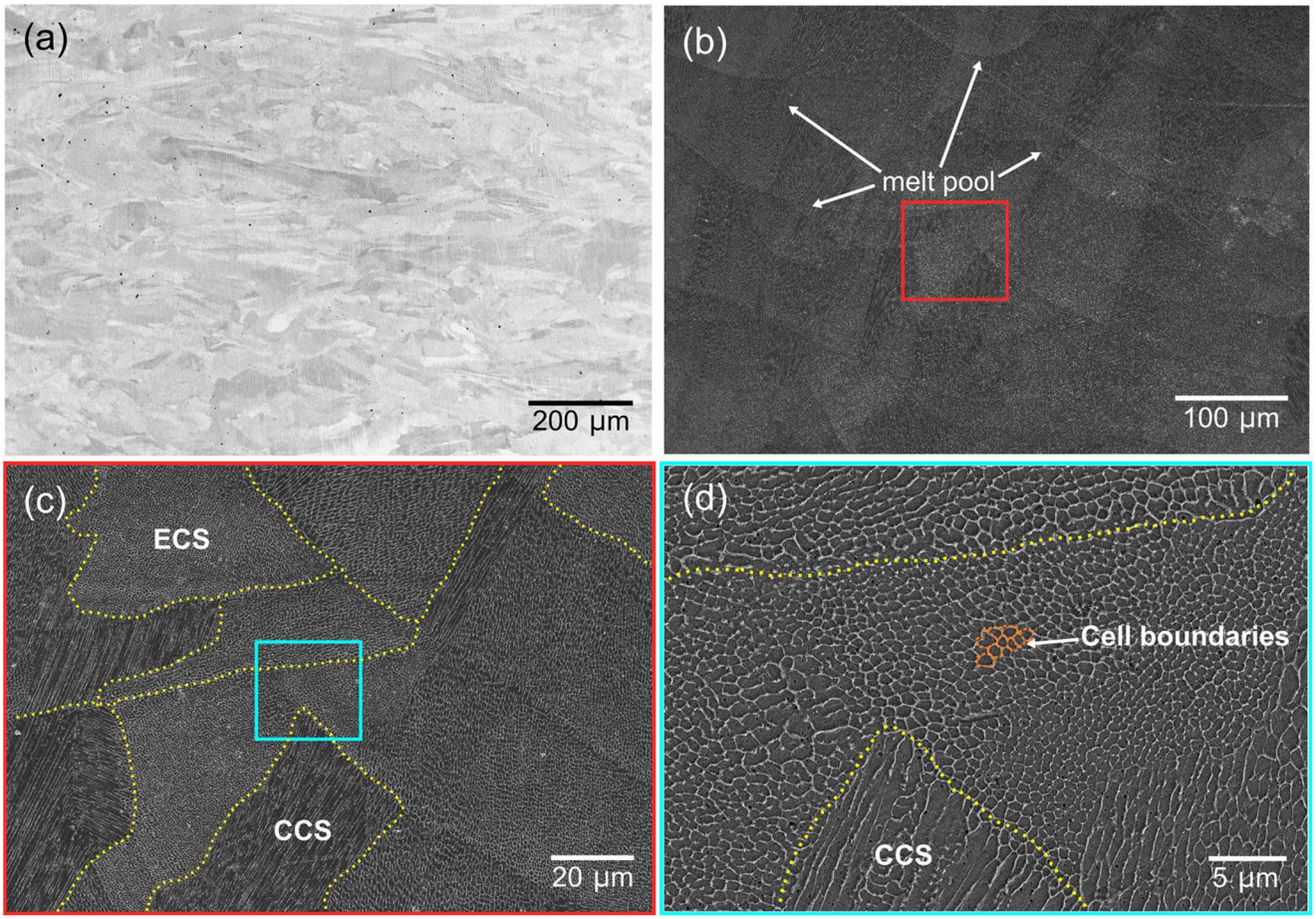

Fig. 3 (**a**) Back scattered electron image of unetched AM Ni-free sample. (b to d) secondary electron micrographs for the etched samples showing characteristic features of the additive manufacturing process. The regions in boxes in (**b**) and (**c**) are zoomed in the (**c**) and (**d**) images, respectively. ECS: Equiaxed cellular structure, CCS: Columnar cellular structure. The micrograph plane is perpendicular to build direction

manufactured 316L stainless steel. Compared to conventional Ni-free austenite, the additively manufactured Ni-free austenite has a modest increase in yield strength due to both interstitial strengthening and an increase in YS_0. The increased cooling rates in PBF-LB AM compared to conventional processing methods allow for supersaturation of N and C, and decrease the size of microstructural features, both enhancing the material's strength.

The hardening behavior of Ni-free alloy and SS316L, in both the PBF-LB and wrought conditions, were fit with the Swift Law:

$$\bar{\sigma} = A\left(\bar{\epsilon}^{p} + \epsilon_0\right)^{n} \tag{2}$$

where $\bar{\epsilon}^{p}$ is the plastic strain, $\bar{\sigma}$ is the von Mises equivalent stress, A is the strength coefficient, n is the strain hardening exponent, and ε_0 is the pre-strain. The hardening parameters are tabulated in Table 3, and the experimentally determined work hardening rates as a function of plastic strain are compared in Fig. 7b. While AM Ni-free has a lower work hardening rate than its conventional counterpart, the difference is less pronounced with increasing plastic strain. This relation is significantly different than the behavior of SS316L, where PBF-LB results in a significant reduction in work hardening rate compared to conventionally processed material.

4 Discussion

Microstructural observations of the AM Ni-free alloy show a fully austenitic structure with the presence of Mn-Si-O particles. Corrosion tests consisting of CPP tests and observation after immersion in $FeCl_3$ demonstrated higher corrosion resistance of the AM Ni-free alloy when compared to wrought 316L stainless steel. A breakdown potential of ~1187 mV_{SCE} was observed in AM Ni-free stainless steel against ~546 mV_{SCE} for W-316L and a repassivation potential of ~1015 mV_{SCE}, against ~129 mV_{SCE} for W-316L. The improved pitting resistance can be attributed to the

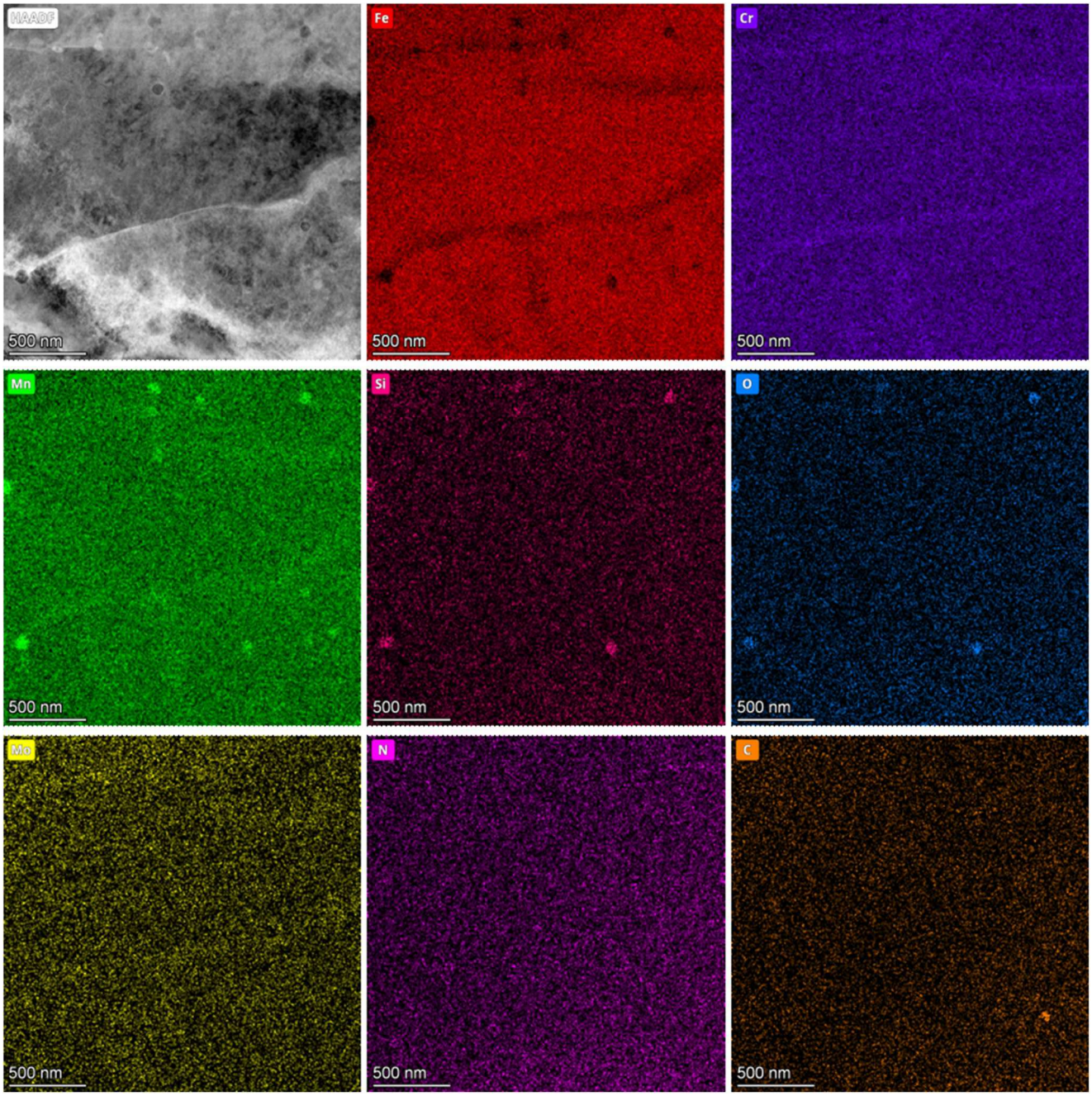

Fig. 4 High angle annular dark field (HAADF) image for the AM Ni-free sample along with elemental mapping, showing the distribution of Mn-Si-O rich particles

combined effect of high N and C content, along with the unique microstructure of additively manufactured alloys. Both N and C occupy interstitial sites in austenite, and the presence of such local covalent bonds may contribute to reducing the metal dissolution rate. Notably, such a mechanism of improving pitting resistance has been proposed for carburized stainless steels [38–40]. The AM Ni-free stainless steel contains high N (~0.6 wt%) and a total of nearly 1 wt% (C+N) interstitial elements against the maximum Limit of 0.15 wt% found in conventional AISI 316L. This underscores an important benefit of additive manufacturing in enabling the production of austenitic stainless steels with higher C+N contents.

Regardless of the amounts of total interstitial element content, the presence of even small amount of N is beneficial. N plays an effective role in improving passivation behavior by providing a buffering action, irrespective of any nitride formation in passive film [19, 41]. Such a buffering

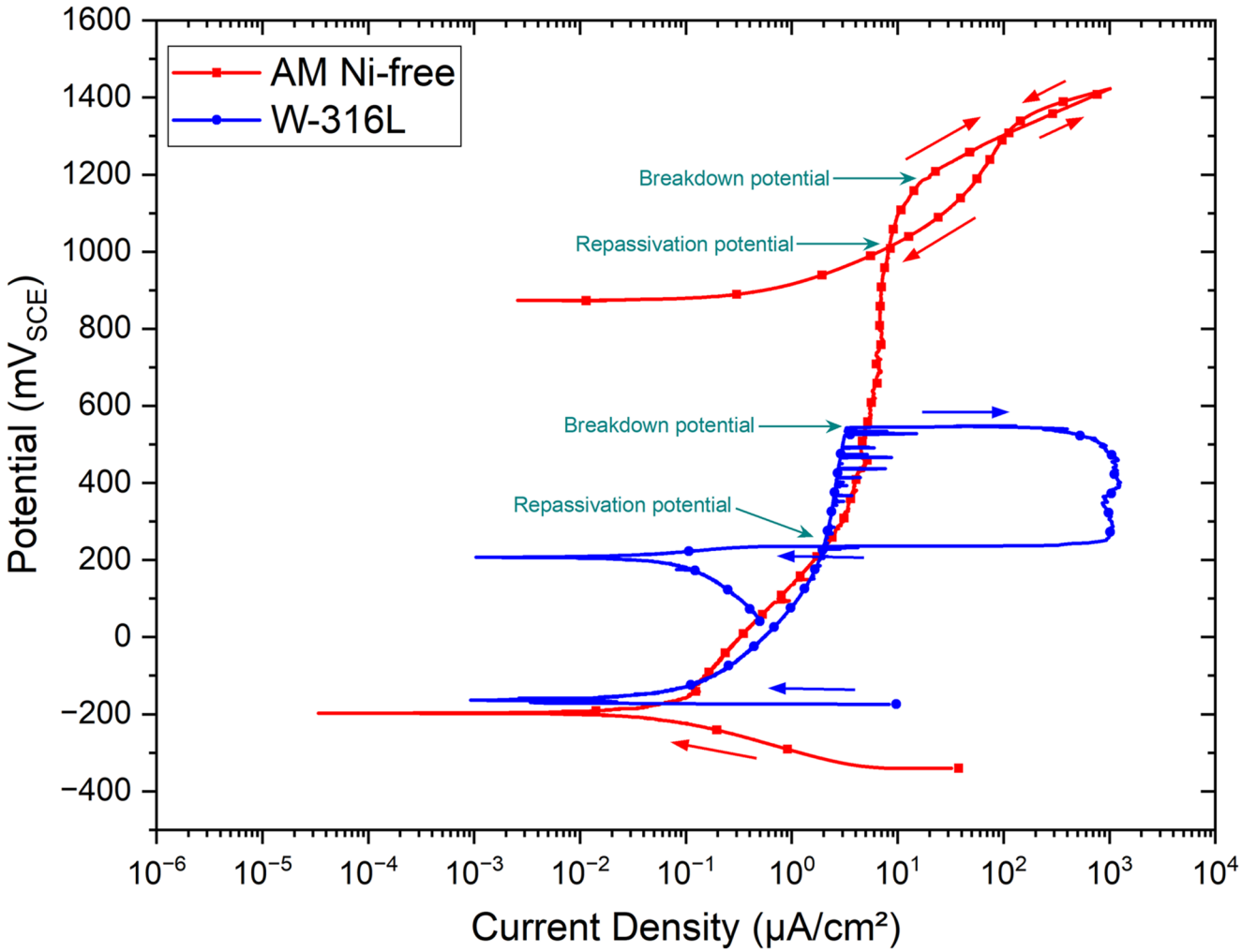

Fig. 5 Cyclic potentiodynamic polarization plots for the AM Ni-free compared to the W-316L stainless steel in 3.5 wt% NaCl solution

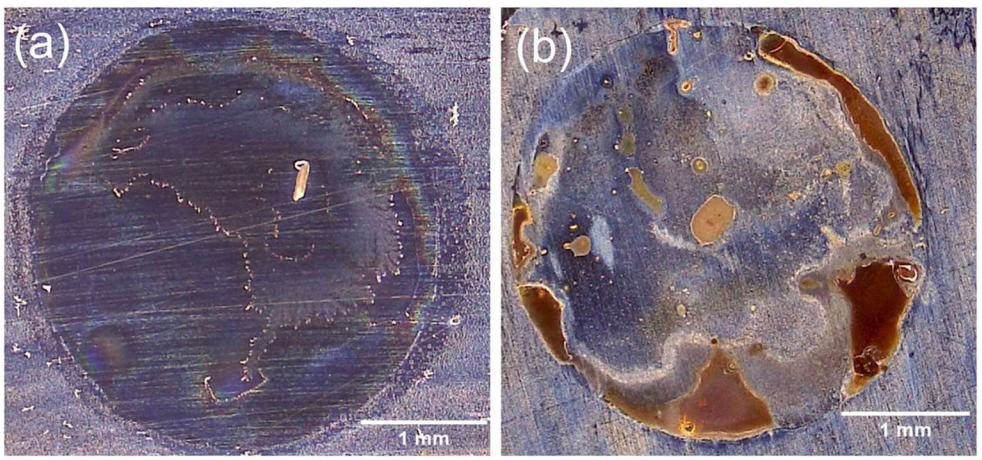

Fig. 6 Stereomicroscopic images of (**a**) AM Ni-free and (**b**) W-316L stainless steel samples after $FeCl_3$ testing

action of N can also potentially explain the improved repassivation tendency observed in high N steels [10, 13]. In context of additive manufacturing, it can be hypothesized that the distribution of N is more uniform than conventional processing in the entire volume of the material, which improves the buffering action of N due to two reasons: first, components in additive manufacturing are built layer by layer with the variations in feed material composition being very minimal. In contrast, N is introduced via surfaces in conventional production routes, leading to a less

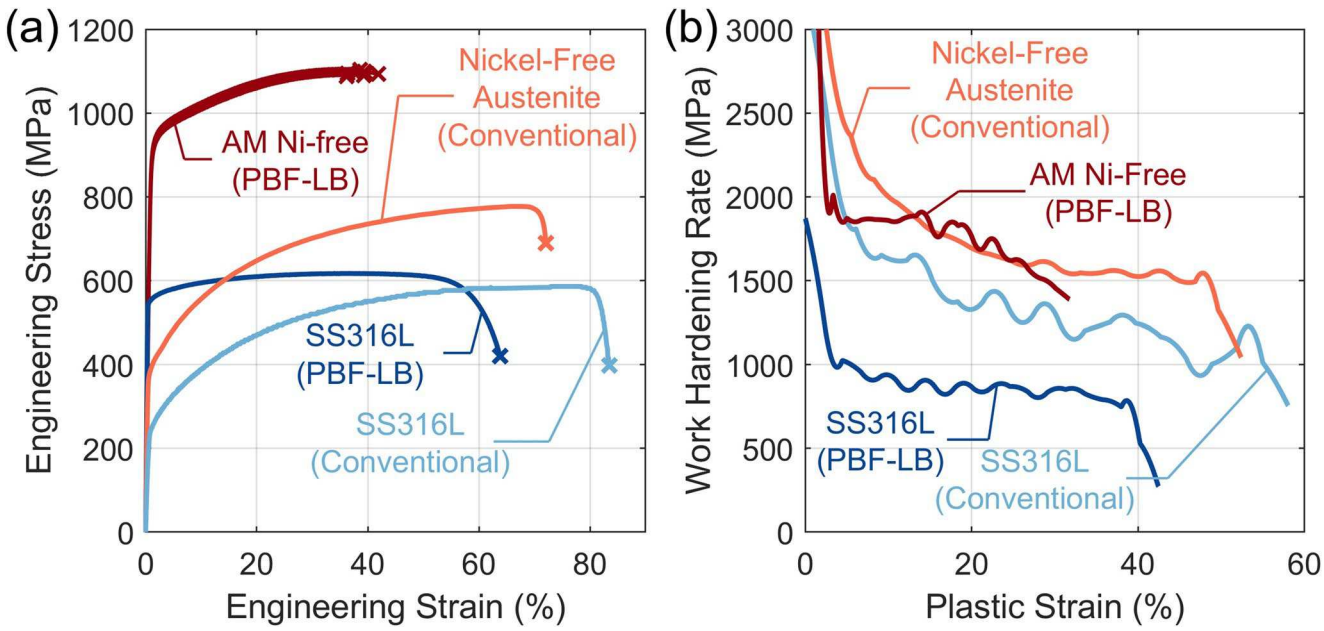

Fig. 7 Comparison of (**a**) engineering stress-strain behavior and (**b**) work hardening rate between Ni-free austenite and SS316L, for both PBF-LB and conventionally processed materials [33–35]

Table 2 Comparison of mechanical properties of Ni-free austenite with SS316L, for both PBF-LB and conventionally processed materials

Material	Fabrication Method	Reference	Yield Strength (MPa)	YS_o (Eq. 1) (MPa)	Interstitial Strengthening (Eq. 1) (MPa)	Ultimate Tensile Strength (MPa)	Engineering Strain at Fracture (%)
AM Ni-free	PBF-LB	This study	860±6	482	378	1098±8	39±2
Low-Ni austenite	Conventional (Annealed)	[37]	540	344	196	830	45
SS316L	PBF-LB	[34]	513±18	483	30	617±3	64±1
SS316L	Conventional (Annealed)	[35]	235±20	205	30	585±20	86±3

Table 3 Comparison of hardening parameters of Ni-free austenite with SS316L, for both PBF-LB and conventionally processed material

Material	Fabrication Method	Reference	A (MPa)	n (-)	ε_0 (-)
AM Ni-free	PBF-LB	This study	2120	0.54	0.219
Ni-free austenite	Conventional (Annealed)	[33]	1760	0.61	0.081
SS316L	PBF-LB	[34]	960	0.99	0.568
SS316L	Conventional (Annealed)	[35]	1380	0.66	0.076

homogenous distribution. Second, the significantly higher cooling rate associated with additive manufacturing rapidly reduces the mobility of N as the material cools [42]. Both factors will potentially lead to more uniform N distributions in additively manufactured alloys compared to those fabricated using conventional processes.

To understand the importance of producing Ni-free, high N stainless steels via additive manufacturing in terms of corrosion behavior, an Ashby type plot of pitting potential and yield strength for different stainless steels is shown in Fig. 8. To construct this figure, values of yield strength were taken from ASM Handbook Volume 2 [43], and the corresponding value for pitting potentials in 3.5 wt% NaCl were taken from various published works [44–53]. All the values (except for the AM Ni-free alloy, shown as a half-filled hexagon) are for wrought alloys. It is evident from the plot that most of the high strength stainless steels, namely, martensitic and precipitate hardenable alloys, exhibit lower pitting potentials, indicating their susceptibility to localized attacks. While duplex stainless steels show exceptional pitting resistance, they offer only limited improvement in terms of yield strength compared to austenitic and ferritic grades. This shows that the development of stainless steels that achieve both high strength and high pitting resistance is an important challenge. The additive manufacturing of austenitic stainless steels, like the one here (AM Ni-free), offers a simultaneous and significant improvement of both pitting resistance and yield strength.

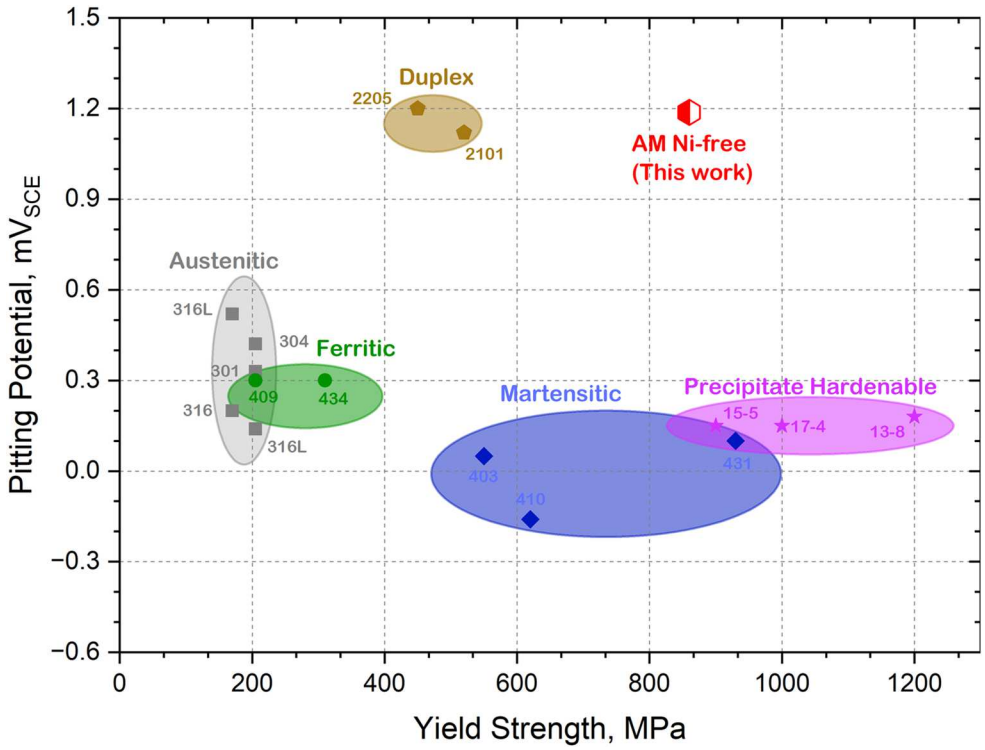

Fig. 8 Material selection chart (Ashby plot) showing the pitting potential and yield strength of AM Ni-free steel among various stainless steels. The pitting potentials in 3.5 wt% NaCl were taken from [44–53]

Table 4 CALPHAD calculations for temperatures at which intermetallic and carbide phases are stable in equilibrium with at least 1 wt.%. Phases stable at room temperature are labeled "RT"

Phase	Ni-free austenite	Low-Ni austenite [37]	SS316L
$M_{23}C_6$	RT – 1025°C	RT – 795°C	RT – 985°C
σ	RT – 820°C	RT – 770°C	430–505°C
M_6C	RT – 435°C	Not stable	Not stable
π	Not stable	Not stable	265–345°C
P	Not stable	Not stable	260–330°C

One challenge with increasing the amount of interstitial C and N compared to low-Ni austenite [37] or SS316L is the increased propensity to form embrittling intermetallic phases or carbides. Equilibrium phase compositions were calculated using the calculation of phase diagrams (CALPHAD Thermo-Calc 2016b) approach with the TCFE8 database, and the temperatures at which intermetallic and carbide phases are predicted to exceed 1 wt% at equilibrium are tabulated below. Compared to conventionally processed low-Ni austenite, the increased interstitial concentration increases the stable temperature of the $M_{23}C_6$ phase by 230°C. Compared to SS316L, the formation temperature for σ-phase is increased by 315°C. Due to increased diffusion rates at these elevated temperatures, the likelihood for forming deleterious phases is greater for the Ni-free composition in this study compared to either conventionally processed low-Ni austenite or SS316L. However, none of the embrittling phases in Table 4 were detected with XRD, as shown in Fig. 2, indicating that the cooling rate of PBF-LB is sufficiently rapid to preclude formation of these phases.

The strength-ductility tradeoff for Ni-free steel and SS316L is compared in Fig. 9. Because wrought alloys are typically cold-worked prior to application, a locus of points for the conventional alloys are shown for various amounts of cold-work. While for SS316L, the PBF-LB material lies near the strength-ductility values that can be obtained with cold-working of conventional material, the PBF-LB fabricated Ni-free sample has a combination of strength and ductility that cannot otherwise be obtained by cold-working a low-nickel austenite.

5 Conclusion

A Ni-free austenitic stainless steel with high N and Mn (AM Ni-free) was fabricated using PBF-LB and exhibited an attractive combination of high strength and excellent corrosion resistance. Microstructural analysis revealed an austenitic matrix with a dispersion of fine Mn-Si-O particles, along with distinct melt pools and a cellular structure. The AM Ni-free alloy exhibited exceptionally higher corrosion resistance as demonstrated by electrochemical testing (a breakdown potential of ~1187 mV_{SCE} and a repassivation potential of ~1015 mV_{SCE}), compared to conventional 316L austenitic stainless steel. Additionally, the ultimate tensile strength for the AM Ni-free alloy was markedly higher than that of its conventional counterpart. These findings highlight the potential for fabricating high strength and corrosion resistant Ni-free austenitic stainless steel through additive manufacturing.

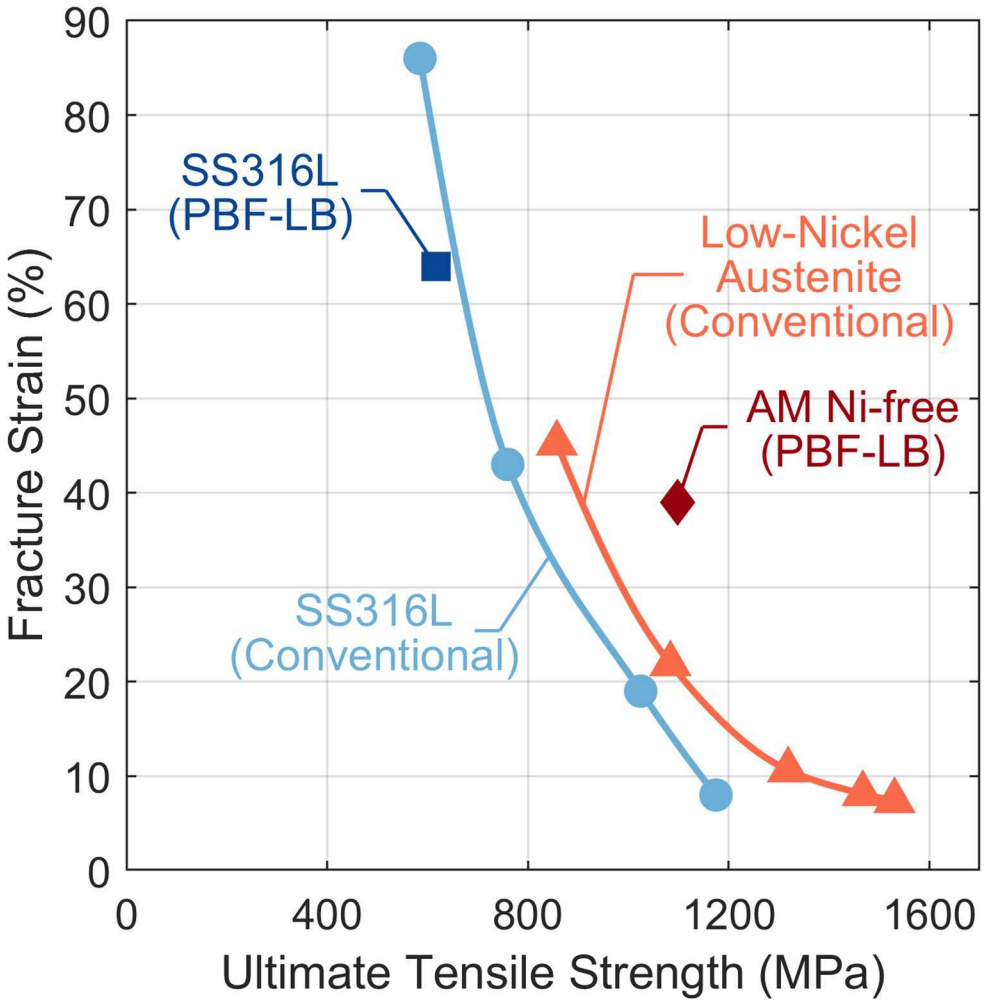

Fig. 9 Comparison of strength-ductility tradeoff between nickel free austenite and SS316L, for both PBF-LB and conventionally processed material. For conventional processing, the strength-ductility tradeoff of both annealed and cold-rolled samples are shown [34, 35, 37]

While this alloy exhibits excellent strength and pitting corrosion resistance, its potential vulnerability to environmentally assisted cracking requires further investigation.

Acknowledgements The authors acknowledge the support of Swiss Steel Group for manufacturing Ni-free powder (commercially available as Printdur® HSA) and printing the test samples. The authors also acknowledge the infrastructure and support received from the Analytical Instrumentation Facility (AIF) at North Carolina State University, which is supported by the State of North Carolina and National Science Foundation (award number ECCS-2025064). The AIF is a member of the North Carolina Research Triangle Nanotechnology Network (RTNN), a site in the National Nanotechnology Coordinated Infrastructure (NNCI).

Author contributions All authors contributed to this study. Andrzej Wojcieszynski and Philipp Kluge supplied the material for this study. Material preparation and preliminary data collection were performed by Sophia Isacco, Sofia Antinozzi, Erik T. Furton, Sean P. O'Brien, Alexabder T. Helmer and Rahul K. Agrawal. Formal analysis and data curation were carried out by Rahul K. Agrawal and Erik T. Furton. The first draft was prepared by Sophia Isacco and Rahul K. Agrawal. Allison M. Beese and Rajeev K. Gupta conceptualized the project, acquired funding, and supervised the execution. All authors read and approved the final manuscript.

Funding This work was supported by the Office of Naval Research under grant number N00014-23-1-2758. Authors AMB and ETF also acknowledge the support received from National Science Foundation (grant number CMMI-1652575).

Declarations

Competing interests The authors declare that they have no competing financial interests or personal relationships that could have appeared to influence the work reported in this paper.

References

1. S.D. Washko, G. Aggen, Wrought Stainless Steels, in Properties and Selection: Irons, Steels, and, High-Performance, Alloys, ASM International, (1990) pp. 841–907. https://doi.org/10.31399/asm.hb.v01.a0001046
2. D.K. Subramanyam, A.E. Swansiger, H.S. Avery, Austenitic Manganese Steels, in Properties and Selection: Irons, Steels, and, High-Performance, Alloys, ASM International, (1990) pp. 822–840. https://doi.org/10.31399/asm.hb.v01.a0001045
3. K. Yang, Y. Ren, Sci. Technol. Adv. Mater. **11**, 014105 (2010). https://doi.org/10.1088/1468-6996/11/1/014105
4. M. Talha, C.K. Behera, O.P. Sinha, Mater. Sci. Eng. C **33**, 3563–3575 (2013). https://doi.org/10.1016/j.msec.2013.06.002
5. R.J. Narayan, ASM International, Medical Applications of Stainless Steels, in Materials for Medical Devices, (, 2012) pp. 199–210. https://doi.org/10.31399/asm.hb.v23.a0005673
6. A.F. Rowcliffe, L.K. Mansur, D.T. Hoelzer, R.K. Nanstad, J. Nucl. Mater. **392**, 341–352 (2009). https://doi.org/10.1016/j.jnucmat.2009.03.023
7. K. Jin, W. Guo, C. Lu, M.W. Ullah, Y. Zhang, W.J. Weber, L. Wang, J.D. Poplawsky, H. Bei, Acta Mater. **121**, 365–373 (2016). https://doi.org/10.1016/j.actamat.2016.09.025
8. M.W. Ullah, D.S. Aidhy, Y. Zhang, W.J. Weber, Acta Mater. **109**, 17–22 (2016). https://doi.org/10.1016/j.actamat.2016.02.048
9. O. Bouaziz, S. Allain, C.P. Scott, P. Cugy, D. Barbier, Curr. Opin. Solid State Mater. Sci. **15**, 141–168 (2011). https://doi.org/10.1016/j.cossms.2011.04.002
10. F. Gao, Y. Qiao, J. Chen, L. Yang, H. Zhou, Z. Zheng, L. Zhang, Npj Mater. Degrad. **7**, 1–14 (2023). https://doi.org/10.1038/s41529-023-00394-x
11. W.-F. Wang, Corros. Sci. **45**, 957–966 (2003). https://doi.org/10.1016/S0010-938X(02)00181-6
12. J.B. Lee, S.I. Yoon, Mater. Chem. Phys. **122**, 194–199 (2010). https://doi.org/10.1016/j.matchemphys.2010.02.033
13. J. Dai, H. Feng, H.B. Li, Z.H. Jiang, H. Li, S.C. Zhang, P. Zhou, T. Zhang, Corros. Sci. **174**, 108792 (2020). https://doi.org/10.1016/j.corsci.2020.108792
14. H. Baba, T. Kodama, Y. Katada, Corros. Sci. **44**, 2393–2407 (2002). https://doi.org/10.1016/S0010-938X(02)00040-9
15. Y.S. Lim, J.S. Kim, S.J. Ahn, H.S. Kvvon, Y. Katada, Corros. Sci. **43**, 53–68 (2001). https://doi.org/10.1016/S0010-938X(00)00074-3
16. J.W. Simmons, Mater. Sci. Eng. A **207**, 159–169 (1996). https://doi.org/10.1016/0921-5093(95)09991-3
17. Y. Fu, X. Wu, E.H. Han, W. Ke, K. Yang, Z. Jiang, Electrochim. Acta. **54**, 4005–4014 (2009). https://doi.org/10.1016/j.electacta.2009.02.024
18. S. Ningshen, U. Kamachi Mudali, V.K. Mittal, H.S. Khatak, Corros. Sci. **49**, 481–496 (2007). https://doi.org/10.1016/j.corsci.2006.05.041
19. R.F.A. Jargelius-Pettersson, Corros. Sci. **41**, 1639–1664 (1999). https://doi.org/10.1016/S0010-938X(99)00013-X
20. Z. Li, J. Li, W. Zhu, J. Jiao, B. Wang, Y. Tian, X. Yang, L. Yang, H. Liu, B. Wang, Corros. Sci. **247**, 112778 (2025). https://doi.org/10.1016/j.corsci.2025.112778
21. T. DebRoy, H.L. Wei, J.S. Zuback, T. Mukherjee, J.W. Elmer, J.O. Milewski, A.M. Beese, A. Wilson-Heid, A. De, W. Zhang, Prog Mater. Sci. **92**, 112–224 (2018). https://doi.org/10.1016/j.pmatsci.2017.10.001
22. T. Furumoto, K. Oishi, S. Abe, K. Tsubouchi, M. Yamaguchi, A.T. Clare, J. Mater. Process. Technol. **299**, 117384 (2022). https://doi.org/10.1016/j.jmatprotec.2021.117384
23. V.B. Vukkum, J. Christudasjustus, A.A. Darwish, S.M. Storck, R.K. Gupta, Npj Mater. Degrad. **6**, 1–11 (2022). https://doi.org/10.1038/s41529-021-00215-z
24. V.B. Vukkum, A.A. Darwish, A. Choudhari, Z. Yang, S.M. Storck, T. Borkar, R.K. Gupta, J. Mater. Eng. Perform. (2025). https://doi.org/10.1007/s11665-025-11102-y
25. B. Cheng, F. Wei, W.H. Teh, J.J. Lee, T.L. Meng, K.B. Lau, L.T. Chew, Z. Zhang, K.H. Cheong, C.K. Ng, P. Wang, C.C. Tan, U. Ramamurty, Addit. Manuf. **55**, 102810 (2022). https://doi.org/10.1016/j.addma.2022.102810
26. L.A. Tochiro, A.H.G. Gabriel, M. Terada, R.S. de Castro, É.S.N. Lopes, J.A. Avila, M. Masoumi, Int. J. Adv. Manuf. Technol. **131**, 1377–1396 (2024). https://doi.org/10.1007/s00170-024-13073-1
27. V.B. Vukkum, J. Christudasjustus, T.Y. Ansell, A. Nieto, R.K. Gupta, Corros. Sci. **224**, 111494 (2023). https://doi.org/10.1016/j.corsci.2023.111494
28. B. AlMangour, Y.-K. Kim, D. Grzesiak, K.-A. Lee, Compos. Part. B Eng. **156**, 51–63 (2019). https://doi.org/10.1016/j.compositesb.2018.07.050
29. Y. Zhong, L. Liu, S. Wikman, D. Cui, Z. Shen, J. Nucl. Mater. **470**, 170–178 (2016). https://doi.org/10.1016/j.jnucmat.2015.12.034
30. S. Esmailzadeh, M. Aliofkhazraei, H. Sarlak, Prot. Met. Phys. Chem. Surf. **54**, 976–989 (2018). https://doi.org/10.1134/S2070205118050026X
31. M. Atapour, H. Sarlak, M. Esmailzadeh, Int. J. Adv. Manuf. Technol. **83**, 721–728 (2016). https://doi.org/10.1007/s00170-015-7601-5
32. E. McCafferty, *Introduction to Corrosion Science* (Springer, New York, New York, NY, 2010). https://doi.org/10.1007/978-1-4419-0455-3
33. M. Pozuelo, J.E. Wittig, J.A. Jiménez, G. Frommeyer, Metall. Mater. Trans. A **40**, 1826–1834 (2009). https://doi.org/10.1007/s11661-009-9863-8
34. A.E. Wilson-Heid, S. Qin, A.M. Beese, Acta Mater. **199**, 578–592 (2020). https://doi.org/10.1016/j.actamat.2020.08.066
35. M. Odnobokova, Z. Yanushkevich, R. Kaibyshev, A. Belyakov, Mater. (Basel). **13**, 2116 (2020). https://doi.org/10.3390/ma13092116
36. C.M. Hsiao, E.J. Dulis, Trans. Am. Soc. Met. **52**, 855–877 (1960)
37. J.J. Heger, Mechanical Properties and Corrosion Resistance of a High-Strength Chromium-Manganese-Nitrogen-Stainless Steel, in *Advances in the Technology of Stainless Steels and Related Alloys*. (ASTM International, 100 Barr Harbor Drive, PO Box C700, West Conshohocken, PA 19428–2959, 1965), pp.54–61. https://doi.org/10.1520/STP43732S
38. W. Niu, R.S. Lillard, Z. Li, F. Ernst, Electrochim. Acta. **176**, 410–419 (2015). https://doi.org/10.1016/j.electacta.2015.06.102
39. T. Li, S.-C. Chien, Z. Ren, W. Windl, F. Ernst, G.S. Frankel, Acta Mater. **221**, 117433 (2021). https://doi.org/10.1016/j.actamat.2021.117433
40. H.Y. Ha, T.H. Lee, C.S. Oh, S.J. Kim, Scr. Mater. **61**, 121–124 (2009). https://doi.org/10.1016/j.scriptamat.2009.03.018
41. I. Olefjord, L. Wegrelius, Corros. Sci. **38**, 1203–1220 (1996). https://doi.org/10.1016/0010-938X(96)00018-2
42. C.E. Campbell, M.R. Stoudt, F. Zhang, ASM International, Additive Manufacturing of Steels and Stainless Steels, in Additive Manufacturing Processes, (, 2020) pp. 346–365. https://doi.org/10.31399/asm.hb.v24.a0006566
43. Properties, Selection : Irons, Steels, and High-Performance Alloys, (ASM, International, 1990). https://doi.org/10.31399/asm.hb.v01.9781627081610
44. C. Jeong, J.H. Shin, B.S. Kong, J. Chen, Q. Xiao, C. Jang, Y.-J. Kim, Nucl. Eng. Technol. **56**, 2131–2140 (2024). https://doi.org/10.1016/j.net.2024.01.021
45. R.L. Liu, B. Yi, Z. Li, Q.L. Liu, Surf. Interfaces. **62**, 106216 (2025). https://doi.org/10.1016/j.surfin.2025.106216

46. M. Mohammadi, L. Choudhary, I.M. Gadala, A. Alfantazi, J. Electrochem. Soc. **163**, C883–C894 (2016). https://doi.org/10.1149/2.0841614jes
47. B. Martínez-Aparicio, D. Martínez-Bastidas, C. Gaona-Tiburcio, U. Martin, J. Cabral-Miramontes, F. Almeraya-Calderón, J. Solid State Electrochem. **27**, 2993–3001 (2023). https://doi.org/10.1007/s10008-023-05593-9
48. B. Martínez-Aparicio, C. Gaona-Tiburcio, F. Almeraya-Calderon, R. Goldsberry, H. Castaneda, Mater. (Basel). **17**, 4060 (2024). https://doi.org/10.3390/ma17164060
49. I. Taji, M.H. Moayed, M. Mirjalili, Corros. Sci. **92**, 301–308 (2015). https://doi.org/10.1016/j.corsci.2014.12.009
50. R.T. Loto, O. Aluya, Int. J. Adv. Manuf. Technol. **104**, 4341–4351 (2019). https://doi.org/10.1007/s00170-019-04285-x
51. M. Azzi, M. Benkahoul, J.E. Klemberg-Sapieha, L. Martinu, Surf. Coat. Technol. **205**, 1557–1563 (2010). https://doi.org/10.1016/j.surfcoat.2010.08.155
52. A. Pardo, M.C. Merino, A.E. Coy, F. Viejo, R. Arrabal, E. Matykina, Corros. Sci. **50**, 1796–1806 (2008). https://doi.org/10.1016/j.corsci.2008.04.005
53. J. Villegas-Tovar, C. Gaona-Tiburcio, M. Lara-Banda, E. Maldonado-Bandala, M.A. Baltazar-Zamora, J. Cabral-Miramontes, D. Nieves-Mendoza, J. Olguin-Coca, F. Estupiñan-Lopez, F. Almeraya-Calderón, Met. (Basel). **13**, 835 (2023). https://doi.org/10.3390/met13050835